

# Performance of new silica aerogels in a threshold Čerenkov counter

---

**D. Blyth<sup>a\*</sup>, R. Alarcon<sup>a</sup>, R. Begag<sup>b</sup>, J. Holmes<sup>a</sup>, and J. Stryker<sup>a</sup>**

*<sup>a</sup>Department of Physics, Arizona State University,*

*Tempe, AZ 85287-1504, U.S.A.*

*E-mail: dblyth@asu.edu*

*<sup>b</sup>Aspen Aerogels, Inc.,*

*Northborough, MA 01532, U.S.A.*

**ABSTRACT:** New highly transparent, hydrophobic silica aerogels with refractive indices of 1.01 to 1.07 have been produced by Aspen Aerogels, Inc., and select tiles have been tested using an electron beam at the DESY, Hamburg facility. A diffusively-reflective threshold Čerenkov counter was designed and constructed for the purpose of evaluating the aerogels, and can accommodate aerogel tile areas of up to 20 cm by 20 cm. Measurements of the performance of the counter using the new aerogels as Čerenkov radiators are given in terms of photoelectron yields and a figure of merit.

**KEYWORDS:** Particle identification methods, Cherenkov detectors.

---

\*Corresponding Author

---

## Contents

<b>1. Introduction</b>	<b>1</b>
<b>2. Silica aerogels</b>	<b>2</b>
2.1 Sol-gel chemistry	2
2.2 Aging process	3
2.3 Supercritical drying	3
2.4 Refractive index	3
<b>3. Experimental setup</b>	<b>4</b>
3.1 Čerenkov Counter	4
3.2 Data acquisition	5
3.3 Test beam	5
<b>4. Signal analysis</b>	<b>6</b>
4.1 Pulse binning	6
4.2 Determination of average photoelectron counts	8
4.2.1 Deconvolution	8
4.2.2 Pedestal integration	9
<b>5. Figure of Merit</b>	<b>9</b>
<b>6. Aerogel configurations and results</b>	<b>10</b>
6.1 Large tile performance	11
<b>7. Summary</b>	<b>12</b>

---

## 1. Introduction

Silica aerogels perform a vital role in nuclear and particle physics experiments as radiators for Čerenkov detectors. These aerogels cover a range of refractive index from about 1.01 to 1.08, and can be both highly transparent and hydrophobic. The often-large volume of aerogel required for experiments can be very costly, and commercial alternatives to products such as those produced by Matsushita Electric Works could be beneficial. The work presented in this paper is part of an effort to test the performance of new hydrophobic aerogels produced by Aspen Aerogels in prototype Čerenkov detectors, and answers the call for proposals found in the U.S. DOE Small Business Innovation Research (SBIR) Funding Opportunity Announcements (FOAs) (see for example page 103 of Phase I Release 1 found in [1]). The SBIR FOAs call for cost-effective Čerenkov radiators with indices between those of gases and liquids, e.g., aerogels. The ultimate goal is the qualification of

commercially produced, cost-efficient, and high-quality aerogel for use in the physics community by benchmarking the performance of the aerogel in both threshold and ring-imaging Čerenkov detectors. In this paper, we report on aerogel production and testing performed using a threshold-type counter.

A number of aerogel tiles have been produced by Aspen Aerogels, and a small selection have been used for testing in the research presented here. A summary of the techniques used in the production of the aerogels is given in section 2 along with a description of the technique used for measuring the refractive index of the tiles. In this section, we also present the distribution of refractive index measurements taken.

The performance testing was achieved by measuring the performance of a prototype Čerenkov threshold counter using the new aerogels. Quantification of the performance is given in terms of both photoelectron yield from the photomultiplier tubes (PMTs) that view the counter, as well as calculated figures of merit. This approach is an alternative to measuring individual optical properties of the aerogel, and instead aims to provide a benchmark in the context of Čerenkov particle detection. The prototype counter was evaluated using an electron test beam at DESY, Hamburg. Details of the experimental setup and test beam can be found in section 3.

Analysis of the experimental data is discussed in section 4, where a variation on a common and robust method of photoelectron quantification is presented. The analysis focuses on determination of the relative inefficiency of detecting electrons in order to extrapolate to average photoelectron yield using the application of Poisson statistics. This avoids difficulties often encountered when complex PMT responses are fit. Another desirable feature of this approach is that it provides a means of measuring systematic error in the determination of photoelectron yields.

In section 5 we describe a figure of merit (FoM) intended to quantify performance in a way that is comparable to different geometries. This FoM is derived from, and nearly identical to, that described by D.W. Higinbotham [2], and as such provides a direct comparison to previous experimental results analyzed in [2]. The aerogel configurations tested, with tile sizes up to 20 cm by 20 cm, are described in section 6 along with photoelectron yields and figures of merit. In addition, dependence of the photoelectron yields on aerogel depth and incident beam position are presented and discussed.

## **2. Silica aerogels**

### **2.1 Sol-gel chemistry**

Fabrication of aerogels generally involves two major steps: formation of a wet gel, and drying of the wet gel to form an aerogel. The vast majority of silica aerogels prepared today utilize silicon alkoxide precursors; this route avoids the formation of undesirable salt by-products and allows more control over the final product. The most common alkoxide precursors are tetramethylorthosilicate (TMOS) and tetraethylorthosilicate (TEOS), however, many others can be used to impart different properties to the gel. The reaction is typically performed in ethanol, with the aerogel density dependent on the concentration of alkoxide. Hexamethyldisilazane (HMDZ) is often used during aging of TEOS or TMOS gels to make the silica surface hydrophobic. However, this treatment takes time, and the transparency of the aerogel is affected by the amount of HMDZ. In

this program, a methylsiliconate precursor was used as the co-precursor with TEOS, which showed great results in terms of aerogel hydrophobicity and transparency.

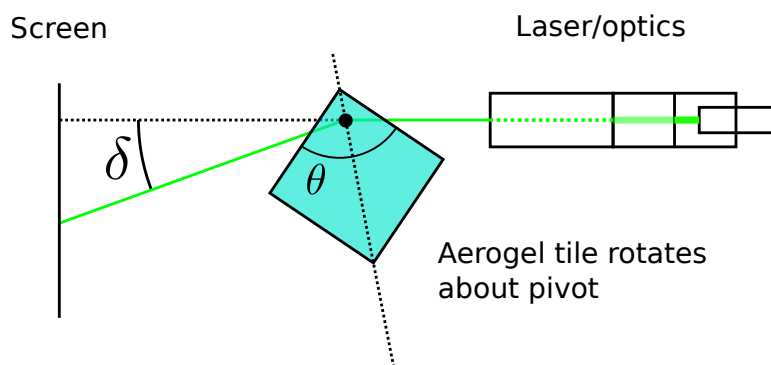
## 2.2 Aging process

It is often assumed that the hydrolysis and condensation reactions of the silicon alkoxides are complete when a sol reaches the gel point, however the silica backbone of the gel still contains a significant number of unreacted alkoxide groups. In fact, hydrolysis and condensation reactions continue after several days beyond the gelation point. Failure to realize and accommodate this is a common mistake preparing silica aerogel monoliths, as weak aerogels will result. Strengthening the gel is a result of the aging process, and is enhanced by controlling the pH and water content of the aging bath. Common aging procedures for base catalyzed gels involve soaking the gel in an alcohol/ammonia mixture, at a pH of 8-9 for up to 48 hours at 60 °C. The time required for this process depends on the gel thickness. Any water left in the gel will not be removed by supercritical drying, and will lead to an opaque, white, and very dense aerogel.

## 2.3 Supercritical drying

The final process step for silica aerogels is supercritical drying. This is where the liquid within the gel is removed, at supercritical conditions, leaving only the linked silica network [3], [4]. The process can be performed by venting the ethanol above its critical point or by prior solvent exchange with CO<sub>2</sub> followed by supercritical CO<sub>2</sub> venting [5], [6]. The gels are put in a high pressure vessel with liquid CO<sub>2</sub> and solvent exchange occurs between ethanol and CO<sub>2</sub>. Once the ethanol is extracted, the gels are brought to the critical point of CO<sub>2</sub> (31.06 °C and 1050 psi) and CO<sub>2</sub> is slowly vented. Once the pressure reaches ambient, the vessel is opened and crack-free aerogel monoliths are obtained. In this program, a 60 liter vessel was used to fabricate the aerogel tiles for optical characterization. Batches of different refractive index were fabricated for Čerenkov detection performance evaluation at Arizona State University.

## 2.4 Refractive index



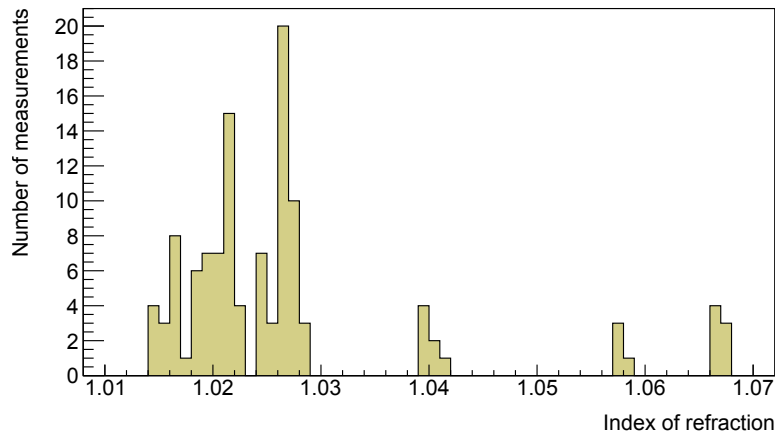
**Figure 1.** A diagram representing the apparatus used to measure refractive indices of the aerogel tiles - The method of measuring the index of refraction for a tile of aerogel makes use of the simple prism effect. This method is very precise for low indices such as those of aerogel.

Figure 1 shows the setup for measuring the index of refraction for a tile of aerogel. The method is common (see [7] and [8] for other accounts), and easily yields precise measurements for low index materials like aerogel. Refractive indices are calculated by measuring the minimum deflection of a laser beam through the corner of an aerogel tile. The relevant relationship is given by the common formula for a prism,

$$n = \frac{\sin \frac{\theta + \delta}{2}}{\sin \frac{\theta}{2}}, \quad (2.1)$$

where  $n$  is the refractive index at the wavelength of the laser,  $\delta$  is the minimum angle of deflection, and  $\theta$  is the prism angle (in this case, about  $\pi/2$ ). The minimum angle is found by measuring the minimum deflection of the laser beam on a ruled screen. The aerogel is pivoted about the intersection of the undeflected laser line, and a line bisecting the corner of the tile. As the aerogel is pivoted back and forth, a minimum deflection is easily found.

The laser used is at a wavelength of 532 nm, and lies comfortably in the spectral range of bialkali photocathodes, such as those used by the photomultiplier tubes in our Čerenkov test counter.



**Figure 2.** Histogram of the refractive index measurements - For each tile, the refractive index was measured using the above method on more than one corner of the tile. The histogrammed data represent the range and distribution of indices produced for evaluation.

In Figure 2, a histogram of all of the refractive index measurements represents the range of indices produced for evaluation. In this paper, measurements of only a portion of the tiles are presented.

### 3. Experimental setup

#### 3.1 Čerenkov Counter

A diffusively reflective threshold counter was developed for testing the new aerogels. It consists of an aluminum light box with dimensions  $36.32 \times 20.32 \times 20$  cm<sup>3</sup> in the  $\hat{x}$ ,  $\hat{y}$ , and  $\hat{z}$  directions respectively (see Figure 3 for axes), a  $20.32 \times 20.32 \times 6.4$  cm<sup>3</sup> box extruded upstream from the light box to house aerogel, and two 5" Photonis XP4500B photomultiplier tubes (PMTs) coupled

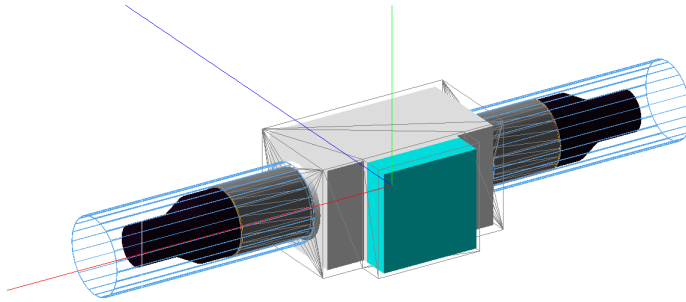


**Figure 3.** Counter Geometry - The solid filled regions in this image represent aerogel (cyan), air surrounded by diffuse reflector (white), aluminum light guides (grey), and PMT mock-ups (black). Represented in wireframe, the aluminum housing (grey) and magnetic shielding (light blue) are also shown. The red, green, and blue axis lines represent the  $\hat{x}$ ,  $\hat{y}$ , and  $\hat{z}$  axes respectively, where the  $\hat{z}$ -axis is parallel to the beam.

to the sides of the light box. A 0.6 mm-thick aluminum window is seen by the beam before passing through the aerogel. The light box and aerogel box are lined on the inside with a white, diffusively reflective “paper”, Millipore GVHP00010. The PMTs are coupled to the light box with polished circular-cylindrical aluminum light guides with an inside diameter of 13.6 cm. The PMTs use a UV glass and a bi-alkali photocathode, and manufacturer’s specifications for the Photonis XP4500B state a peak quantum efficiency of 24%, with a spectral range of about 200 - 650 nm where the efficiency falls off below 10% of peak.

The purpose of the aluminum light guides is to couple the PMTs at a distance so that shielding for static magnetic fields can be effectively used. The test counter is not tested in a significant magnetic field here, but the performance of the counter itself in this configuration is of interest for future applications. In this setup, magnetic shields produced by MuShield are in place which reduce ambient magnetic field at the photocathodes by a factor of 100.

### 3.2 Data acquisition

For readout, we use a 12-bit 250 MS/s digitizer (CAEN V1720). The PMTs coupled with the Photonis VD105k bases produce a signal with a FWHM  $\approx 4$  ns. This is too sharp of a pulse for the digitizer sample rate, so the PMT signals are fed through passive 32 MHz low-pass LC filters. When an external trigger is received, a number of digitized samples recorded in the vicinity of the trigger are stored for offline analysis. These samples include data prior to the trigger, so that a pedestal can be calculated for each event.

### 3.3 Test beam

The T22  $e^-/e^+$  test beam at the DESY facility in Hamburg was used to perform tests of the aerogel/counter combination. The beam is generated by converting bremsstrahlung radiation from carbon fiber targets in the DESY II lepton storage ring. The leptons in this storage ring are bunched, and revolve once every microsecond [9]. For this setup, converted electrons at an energy of 2 GeV are selected, with an energy spread  $\approx 5\%$ . The beam is shaped by a  $20 \times 20$  mm<sup>2</sup> primary collima-

tor, and then a  $6 \times 6 \text{ mm}^2$  secondary collimator. Located immediately downstream of the secondary collimator is a broad scintillator (S1). Approximately 5 m further downstream is the Čerenkov test counter, and another 5 m downstream is a  $2 \times 2 \text{ cm}^2$  scintillator (S2). The test counter was mounted to an X-Y translation table for relative beam positioning, and to measure position dependence. A trigger signal is produced with coincidence between S1 and S2. The average trigger rate is  $\approx 4 \text{ kHz}$ .

For simplicity, it's beneficial to argue that on each trigger, only one electron passes through the counter. Given the trigger rate and the bunched nature of the storage ring, we estimate that there are an average of 1.002 electrons passing through the counter on triggered events. This estimate relies on the assumption that all electrons passing through the counter produce a trigger. Based on the observed narrowness of the beam, this is a reasonable assumption.

## 4. Signal analysis

### 4.1 Pulse binning

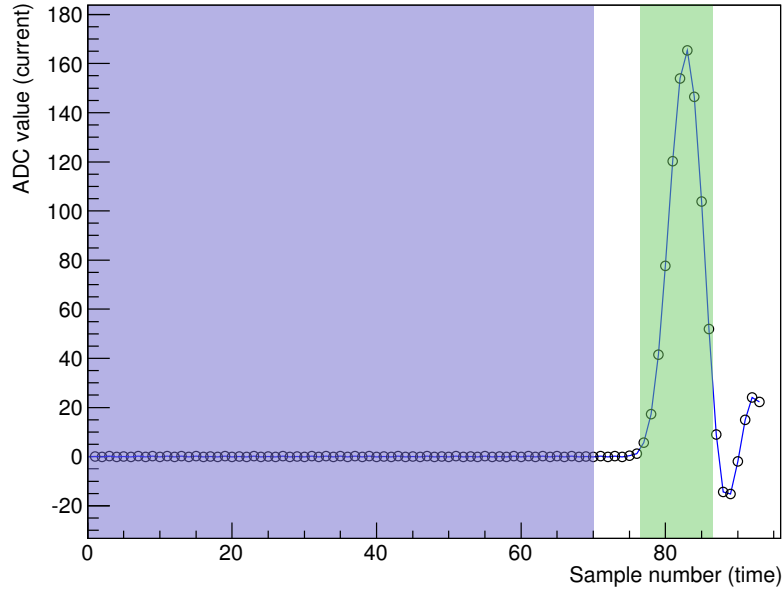


**Figure 4.** PMT Response - An average digitized PMT pulse is shown with the height inverted, so that the pulses discussed here are positive. The region in blue is used to calculate the electronic pedestal for each event. This allows long-term variations in pedestal to be ignored. The region in green is integrated relative to the pedestal for a value proportional to the PMT anode charge.

As described in section 3.2, the PMT waveforms are digitized to be analyzed offline. The timing of the signal is tuned so that 70 samples of electronic pedestal are obtained before the desired PMT signal (Figure 4). The pedestal for each event and for each PMT is therefore amply measured in order to produce a sharp zero-photoelectron peak, on which our analysis ultimately relies. For each event, the latter portion of the waveform in Figure 4 is integrated relative to the calculated pedestal and binned into a pulse-height spectrum (Figure 5). In order to minimize the

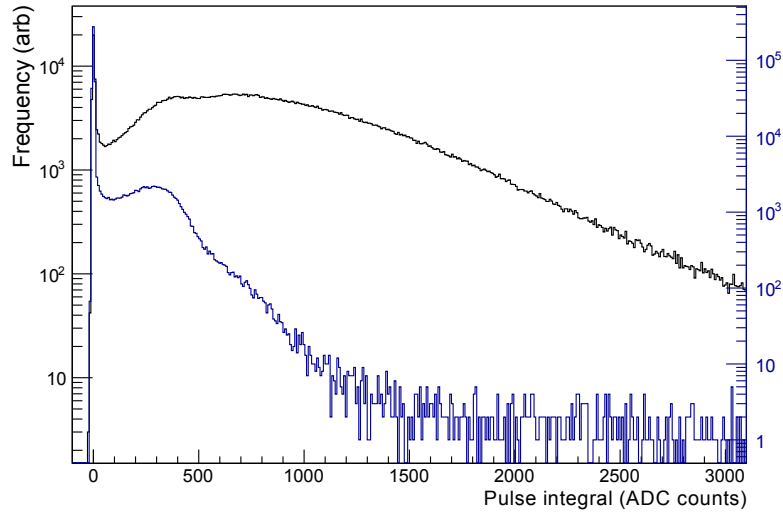


**Figure 5.** Pulse-Height Spectrum - The data shown are generated by binning the measured PMT charge for each triggerable event. The black line represents a measurement with aerogel in the counter, while the blue line represents a measurement with only air in order to identify a single photoelectron peak. The key features are the zero-photoelectron (pedestal) peak on the left, and the single- and multiple-photoelectron bumps to the right. The pedestal peak falls off neatly to zero on the left in a Gaussian fashion, as can be seen in Figure 7.

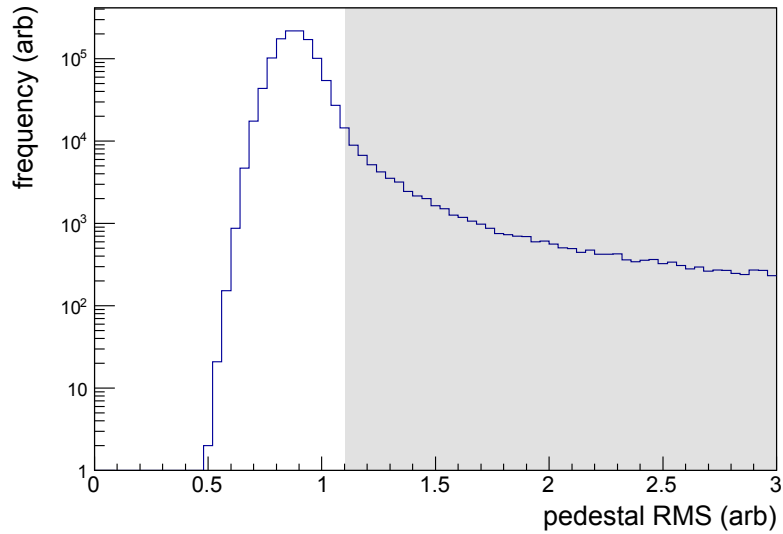


**Figure 6.** Histogram of pedestal RMS values - The desirable Gaussian-like peak of the distribution continues into a region where the tails of thermal dark current pulses begin to dominate the RMS. This produces artifacts in the pedestal calculation which assumes high-frequency stochastic fluctuations. Therefore, a cut is placed on the pedestal RMS (the rejected events shown by the grey region) where the distribution fails to be dominated by such fluctuations. The calculated photoelectron yield has negligible sensitivity to the placement of this cut in the range of 1.0 - 1.2.



effects of dark current, a cut is placed on the standard deviation of the pedestal samples to enforce the assumption of a constant signal with a small random error. This cut, shown in Figure 6, is necessary for minimizing artifacts in the zero-photoelectron peak due to dark current.

## 4.2 Determination of average photoelectron counts

The pulse-height spectrum shown in Figure 5 has a sharp peak at the left corresponding to the absence of photomultiplication, and its integrated value divided by the total number of events is therefore considered to be the probability that zero photoelectrons are produced in the PMT for a triggerable event in a given counter configuration. The probability distribution for the number of photoelectrons emitted from the PMT cathodes in a triggerable event is well approximated by a Poisson, given the low probability of a radiated photon producing a photoelectron. We therefore claim that the average number of photoelectrons produced for such an event is equal to

$$\langle N_{PE} \rangle = -\ln \frac{N_{ped}}{N_{tot}} \quad (4.1)$$

where  $N_{ped}$  and  $N_{tot}$  are the pedestal event and total event counts respectively. This general approach has been compared to other techniques in [10], where R. Dossi et al. also incorporate a model for single- and multiple-photoelectron peaks for a  $\chi^2$  fit to data. We have chosen this approach since it has the advantage of few assumptions, and we have found it to be robust in our application.

Systematic error in the determination of  $N_{ped}$  comes from overlap of the pedestal peak with contributions from non-zero photoelectron signals. This is potentially largely due to incomplete photomultiplication in the large PMTs. In practice, a sharp pedestal peak is necessary and a cutoff is placed on the integration of the pedestal peak and varied to examine systematic effects. As a guide for this cutoff, a method of determining the width of the pedestal peak will be incorporated in order to place the cutoff at an estimated probability of pedestal noise excursions.

### 4.2.1 Deconvolution

To determine the width of the pedestal peak, a deconvolution method is applied to the pulse-height spectrum with an estimated point-spread function (PSF). The PSF is approximated by a Gaussian with an unknown width, and the reconvolved spectrum is fit to the measured spectrum using a least-squares search method over the PSF width parameter. Figure 7 gives an example of the result of such a fit. The purpose of such a process is to gain a precise form of the PSF.

By constraining the deconvolved spectrum to exist in a positive semi-definite range, we can demand that the true charges deposited on the PMT anode are of only one sign (negative, since the sign is inverted for a positive spectrum). This allows the pedestal region of the spectrum to provide a stable constraint on the PSF. In this way, the fitted PSF can be said to represent the random error in the measurement of charge collected by the PMT anode.

An iterative deconvolution approach known as the Lucy-Richardson algorithm is used [11]. This approach provides a straightforward means of obtaining a maximum-likelihood solution while enforcing the condition  $\psi_i \geq 0$ , where  $\psi_i$  represent the discrete values of the deconvolved spectrum.

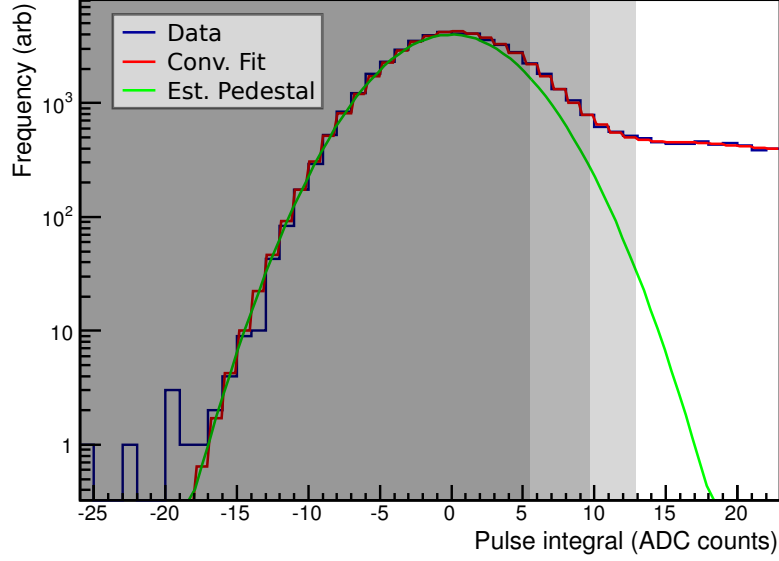


**Figure 7.** Convolution Fit - The data shown are from the zero-photoelectron (pedestal) peak on the left side of Figure 5. The red line represents a reconvolution of the deconvolved spectrum which has been fit to the data to extract the width of the PSF (point-spread function). The reduced  $\chi^2$  of the fit is 102/97. The green line shows the zero pulse-height contribution from the deconvolved spectrum. The three grey regions illustrate the pedestal integration to 90%, 99%, and 99.9% of the total probability (see Equation 4.2).

#### 4.2.2 Pedestal integration

Figure 7 shows the pedestal peak of a pulse-height spectrum along with the predicted pedestal contribution from the deconvolved spectrum. To determine the pedestal contribution from the data, the pulse-height spectrum is integrated from left to right to specific probability intervals based on the fitted PSF. The pedestal integral is taken to be

$$N_{ped,i} = \int_{-\infty}^{\text{erfc}^{-1}[2(1-P_i)]\sqrt{2}\sigma} \tilde{\phi}(x) dx \quad (4.2)$$

where  $\text{erfc}^{-1}$  is the inverse complementary error function –  $P_i$  are 0.9, 0.99, and 0.999 –  $\sigma$  is the width of the Gaussian PSF – and  $\tilde{\phi}(x)$  is the measured spectrum. By combining Equation 4.1 and 4.2,  $P_i$  provide average photoelectron values ( $\langle N_{PE,i} \rangle$ ) for a mid-range result at 99%, and a reasonable range from the upper bound at 90% and the lower bound at 99.9%.

### 5. Figure of Merit

D.W. Higinbotham [2] presents a useful Figure of Merit for threshold Čerenkov counters in the form of

$$H_{D.W.H.} \equiv \frac{\langle N_{PE} \rangle}{L \left(1 - \frac{1}{\beta^2 n^2}\right)} * \frac{1 - \eta (1 - \varepsilon)}{\varepsilon}, \quad (5.1)$$

where  $L$  is the depth of the aerogel,  $\eta$  is the average light box reflectivity (using reasonable values for reflector and aerogel reflectivity given by [2] for uniformity), and  $\varepsilon$  is the fraction of the light

box covered by photosensitive detector. The factor  $L \left(1 - \frac{1}{\beta^2 n^2}\right)$  is approximately proportional to the number of photons radiated from the aerogel, and  $\varepsilon / [1 - \eta (1 - \varepsilon)]$  is the limit of

$$\sum_{n=0}^{\infty} \varepsilon [\eta (1 - \varepsilon)], \quad (5.2)$$

which estimates the probability of a photon reaching a photocathode under the assumption that there is a flat distribution of reflections across the surface of the light box.  $H$  then contains information on light losses in the aerogel, quantum efficiency of photon detectors, and higher-order geometrical effects. In the results of this paper, we will utilize this FoM in a slightly modified form.

Due to the depth of our counter and the rapidity of the beam used for testing, Čerenkov radiation in the air contributes non-trivially to our measured photoelectron yield, making a FoM of the form of Equation 5.1 artificially large. We will account for this by taking

$$L \left(1 - \frac{1}{\beta^2 n^2}\right) \rightarrow L_g \left(1 - \frac{1}{\beta^2 n_g^2}\right) + L_a \left(1 - \frac{1}{\beta^2 n_a^2}\right) \quad (5.3)$$

so that

$$H \equiv \frac{\langle N_{PE} \rangle}{L_g \left(1 - \frac{1}{\beta^2 n_g^2}\right) + L_a \left(1 - \frac{1}{\beta^2 n_a^2}\right)} * \frac{1 - \eta (1 - \varepsilon)}{\varepsilon}, \quad (5.4)$$

where subscripts  $g$  and  $a$  represent aerogel and air respectively. This provides an  $O(10\%)$  correction that reduces the FoM to compare more directly with counters that have less contribution from air.

## 6. Aerogel configurations and results

**Table 1.** Aerogel configuration results - The table below lists for each aerogel configuration the batch number, total aerogel depth, average photoelectron yield, mean refractive index, standard deviation of index measurements, and a Figure of Merit (Equation 5.4) in the style of D.W. Higinbotham [2].

Batch	Depth (mm)	$\langle N_{PE} \rangle$	$\langle n \rangle$	$\sigma_n$	$H$ (cm <sup>-1</sup> )
Empty (air)	0	0.58 <sup>+0.19</sup> <sub>-0.02</sub>	$\approx 1.00028$	N/A	N/A
1	28	3.81 <sup>+0.29</sup> <sub>-0.08</sub>	1.026	0.0016	40
	41	4.91 <sup>+0.32</sup> <sub>-0.10</sub>			36
	56	6.04 <sup>+0.34</sup> <sub>-0.12</sub>			32
2	53	6.36 <sup>+0.34</sup> <sub>-0.12</sub>	1.028	0.0007	34
3	62	5.60 <sup>+0.28</sup> <sub>-0.09</sub>	1.028	0.0023	28

The performance of the Čerenkov threshold test counter has been analyzed with three different batches of aerogel. The batches provide a small spread in refractive index and two different aerogel tile form factors. The tiles from each batch are 1 - 2 cm deep squares.

**Batch 1** has a mean refractive index of 1.026 and has a square area  $\approx 10 \times 10 \text{ cm}^2$ .

**Batch 2** has a mean refractive index of 1.028, and also has a square area  $\approx 10 \times 10 \text{ cm}^2$ .

**Batch 3** also has a mean refractive index of 1.028, but with a square area  $\approx 20 \times 20 \text{ cm}^2$ . This is considered a large tile.

Table 1 lists measurements for a series of aerogel configurations. For each configuration, the total aerogel depth, average number of photoelectrons  $\langle N_{PE} \rangle$ , the mean refractive index, the spread in index measurements, and a Figure of Merit have been calculated. Figure 8 shows a plot of the first four configurations listed in Table 1, along with a fit to the values showing the non-linear depth dependence of Batch 1. This fit is of the form used by I. Adachi et al. [12], and is given by

$$\langle N_{PE} \rangle_d = \langle N_{PE} \rangle_\infty \times \left( 1 - \exp \frac{-d}{L_{eff}} \right) + C, \quad (6.1)$$

where  $d$  is the depth of the aerogel stack, and the effective absorption length  $L_{eff}$  contains information about absorption and scattering in the aerogel convolved with the geometry and reflectivity of the test counter. The spatial dependence of the test counter response with the Batch 3 large tiles has been measured by scanning the counter transversely with respect to the beam, and is shown in Figure 9.

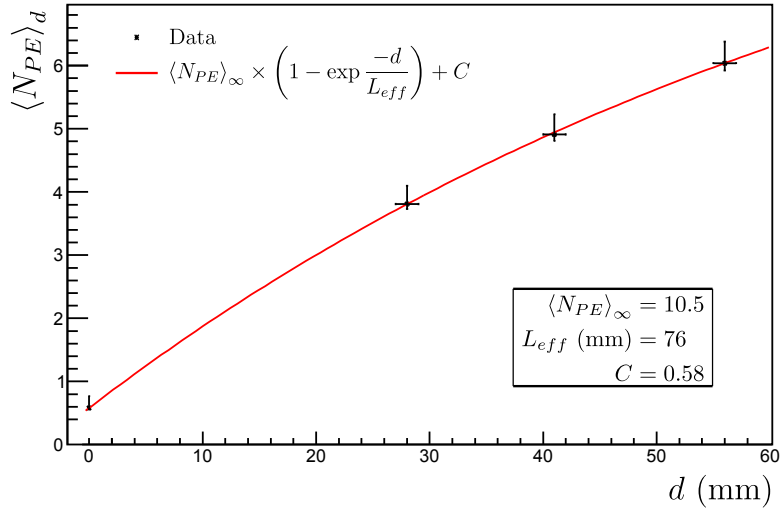


**Figure 8.** Batch 1 depth dependence - The red curve below represents a fit to the data meant to extract the effective aerogel absorption length  $L_{eff}$  and a maximum photoelectron yield for an arbitrarily deep stack of aerogel. The  $\chi^2$  value for the fit is 0.01, which is not unreasonable for a single degree of freedom, but tends to suggest that the systematic errors stated in Table 1 are at high confidence intervals as intended.

## 6.1 Large tile performance

Examining the features in Figure 9, we find that a 1 cm-wide strip of aluminum that was used to hold the aerogel tiles in place during testing produced a significant effect in the spatial scan as indicated by the large dip in the center of the scan. There is also a small asymmetry in the

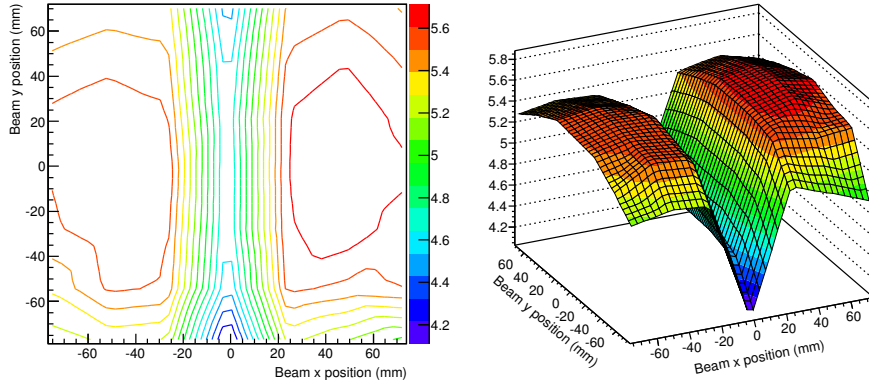


**Figure 9.** Spatial scan - The spatial dependence of the average photoelectron yield  $\langle N_{PE} \rangle$  of the test counter with the Batch 3 large tile configuration is shown below. A large dip down the center is clearly illustrated, which is due to a metal support in the test counter blocking the Čerenkov light cone. A slight preference in the  $+x$  direction exists due to differences in quantum efficiency between the PMTs on either side of the aerogel.

response of the counter on either side of the aluminum support, indicating a difference in quantum efficiencies between the two PMT photocathodes. Finally, a gentle slope exists toward the edges of the scan as a result of the geometry of the light box. A Monte-Carlo simulation was performed which qualitatively replicated each of these features.

The spatial scan shows that the uniformity of the counter in the regions not affected by the aluminum aerogel support is quite good. Each of the measurements listed in Table 1 were obtained with the beam center varying by no more than a few mm relative to the counter, and are each around 50,-50 mm. We conclude that the small variations in relative beam center produced variations between batches in the average number of measured photoelectrons on the order of a percent.

## 7. Summary

Hydrophobic aerogels have been produced for use as Čerenkov radiators in a threshold counter. Measurements of the performance of the aerogel/counter combination with aerogel refractive indices from 1.026 to 1.028 and various depths have been performed, yielding photoelectron counts between 3.8 and 6.4 (Table 1). Using a figure of merit in the style of D.W. Higinbotham [2], low-order effects from the specific refractive indices used – as well as from the geometry (aerogel depth, PMT area, etc) – have been removed to produce values from 28 - 40  $\text{cm}^{-1}$  that can be used to compare to previous experimental results.

## Acknowledgments

This material is based upon work supported by the Department of Energy under Award Number DE-SC0004290 and by the National Science Foundation Awards 0969654 and 1306547. The authors would also like to thank the OLYMPUS collaboration for the beam time at the DESY detector testing facility.

**Disclaimer** This report was prepared as an account of work sponsored by an agency of the United States Government. Neither the United States Government nor any agency thereof, nor any of their employees, makes any warranty, express or implied, or assumes any legal liability or responsibility for the accuracy, completeness, or usefulness of any information, apparatus, product, or process disclosed, or represents that its use would not infringe privately owned rights. Reference herein to any specific commercial product, process, or service by trade name, trademark, manufacturer, or otherwise does not necessarily constitute or imply its endorsement, recommendation, or favoring by the United States Government or any agency thereof. The views and opinions of authors expressed herein do not necessarily state or reflect those of the United States Government or any agency thereof.

## References

- [1] “FY 2015 | U.S. DOE Office of Science (SC).” Web page, November, 2015.
- [2] D. Higinbotham, *Diffusely reflective aerogel cherenkov detector simulation techniques*, *Nucl. Instrum. Methods Phys. Res. A* **414** (1998), no. 2-3 332 – 339.
- [3] S. S. Kistler, E. A. Fischer, and I. R. Freeman, *Sorption and surface area in silica aerogel*, *J. Am. Chem. Soc.* **65** (1943), no. 10 1909–1919, [<http://pubs.acs.org/doi/pdf/10.1021/ja01250a034>].
- [4] M. A. McHugh and V. J. Krukoni, *Supercritical fluid extraction: principles and practice*. Boston: Butterworths, 1986.
- [5] P. Tewari and A. Hunt, *Hydrolysis and condensation of alkoxides to form alcogels; window, appliance insulation*, Sept. 9, 1986. US Patent 4,610,863.
- [6] P. H. Tewari, A. J. Hunt, and K. D. Lofftus, *Ambient-temperature supercritical drying of transparent silica aerogels*, *Mater. Lett.* **3** (1985), no. 9-10 363 – 367.
- [7] Y. K. Akimov, V. P. Zrellov, A. I. Puzynin, S. V. Filin, A. I. Filippov, and V. A. Sheinkman, *An aerogel threshold cherenkov counter*, *Instrum. Exp. Tech.* **45** (2002) 634–639. 10.1023/A:1020497800282.
- [8] Belle Collaboration, S. Sahu, M. Wang, R. Suda, R. Enomoto, K. Peng, C. Wang, I. Adachi, M. Amami, Y. Chang, R. Guo, K. Hayashi, T. Iijima, T. Sumiyoshi, and Y. Yoshida, *Measurement of Radiation Damage on Silica Aerogel Cherenkov Radiator*, *Nucl. Instrum. Methods Phys. Res. A* **A382** (1996) 441–446, [[hep-ex/9604004](http://arxiv.org/abs/hep-ex/9604004)].
- [9] “DESY | Test Beam | Description.” Web page, November, 2015.
- [10] R. Dossi, A. Ianni, G. Ranucci, and O. J. Smirnov, *Methods for precise photoelectron counting with photomultipliers*, *Nucl. Instrum. Methods Phys. Res. A* **451** (2000), no. 3 623–637.
- [11] L. B. Lucy, *An iterative technique for the rectification of observed distributions*, *Astron. J.* **79** (June, 1974) 745+.
- [12] I. Adachi, T. Sumiyoshi, K. Hayashi, N. Iida, R. Enomoto, K. Tsukada, R. Suda, S. Matsumoto, K. Natori, M. Yokoyama, and H. Yokogawa, *Study of a threshold cherenkov counter based on silica aerogels with low refractive indices*, *Nucl. Instrum. Methods Phys. Res. A* **355** (1995), no. 2-3 390 – 398.